

Article

Template-Assisted SnO₂: Synthesis, Composition, and Photoelectrocatalytical Properties

Evgenii Gribov ^{*}, Evgeny Koshevoy, Iuliia Chikunova and Valentin Parmon

Boriskov Institute of Catalysis SB RAS, Pr. Ak. Lavrentieva, 5, 630090 Novosibirsk, Russia

^{*} Correspondence: gribov@catalysis.ru

Abstract: A series of tin oxides were synthesized with polystyrene microspheres (250 nm) as the template. It was shown that an increase in the template content led to increasing specific pore volume and to the formation of bimodal pore structure with pores of 9 and 70 nm in diameter. Addition of cetyltrimethylammonium bromide (CTAB) during synthesis led to the formation of friable structures (SEM data), to an increase in the average pore diameter from 19 to 111 nm, and to the formation of macropores of 80–400 nm in size. All materials had similar surface properties and cassiterite structure with 5.9–10.8 nm coherent scattering region (XRD data). Flat-band potentials of the samples were determined and their photoelectrocatalytic properties to oxidation of water and methanol were studied in the potential range of 0.4–1.6 V RHE. It was shown that the sample obtained using CTAB was characterized by lower flat-band potential value, but appeared significantly higher photocurrent in methanol oxidation, which resulted from enhanced macro-meso-porous structure to facilitate methanol pore diffusion.

Keywords: SnO₂; band-gap; photoelectrocatalysis; template synthesis; XPS; Raman spectroscopy; flat-band potential; photocurrent



Citation: Gribov, E.; Koshevoy, E.; Chikunova, I.; Parmon, V. Template-Assisted SnO₂: Synthesis, Composition, and Photoelectrocatalytical Properties. *Catalysts* **2023**, *13*, 168. <https://doi.org/10.3390/catal13010168>

Academic Editors: Alexander Kokorin and Detlef W. Bahnemann

Received: 30 November 2022

Revised: 29 December 2022

Accepted: 4 January 2023

Published: 11 January 2023



Copyright: © 2023 by the authors. Licensee MDPI, Basel, Switzerland. This article is an open access article distributed under the terms and conditions of the Creative Commons Attribution (CC BY) license (<https://creativecommons.org/licenses/by/4.0/>).

1. Introduction

Tin oxide (TO) is a broad band gap semiconductor. There are a variety of application areas of the material: noble-metal catalyst supports for fuel cells, sensors [1], supercapacitor electrodes [2], clear conducting materials [3], photocatalysts [4], and electro- and photoelectrocatalysts for oxidation of organic substrates [5]. TO is widely used as a photocatalyst due to its high stability, oxidation potential, corrosion resistance, and cost efficiency [4]. However, photocatalytic efficiency of conventional SnO₂ is insufficient because of the broad band gap (~3.6 eV) and difficulties in recombination of photogenerated electrons and holes [6].

A number of approaches were used for broadening light absorption range and decreasing recombination: doping with metals (including Sn) and nonmetals, increasing crystal distortions, varying the phase composition (Sn₃O₄), design of photocatalyst composites with heterojunctions, solid solutions of oxides, and morphology control [4]. The efficiency may be improved by introducing new energy levels into the band gap through doping and increasing crystal deficiency or narrowing band gap using solid solutions and tuning phase composition.

However, changing the band gap by doping is not the only factor determining the photocatalytic properties, and system productivity needs further studies [4].

One of the approaches to improve the material efficiency includes the control of the morphology using hierarchical 3D structures of SnO₂. The advantages of such macro-meso-porous material were demonstrated with lithium-ion batteries [7–9], sensors [10–16], catalysis [17], and photoelectrocatalysis [18,19].

Anodization of Sn foil in oxalic acid [20] allows nanochannel porous SnO₂ to be obtained. It was shown that the distinctive porous channel structure of the materials can

increase absorption efficiency and contribute to the transition of photogenerated electrons to surface hydroxide species. The presence of defects in the porous material increases the lifetime of photogenerated charges and photocatalytic activity. The porous structure of the materials plays a key role in photocatalysis. The dependence of photocurrents on pore diameter and oxide width was shown: the more pore diameter, the more photocurrent [21]. The properties could be enhanced due to enlargement of the specific surface area [22] and pore structure optimization [23]. Furthermore, light scattering in mesoporous space between nanoparticles favors better material light absorption [24].

One of the ways to achieve pore formation is the use of templates during the material synthesis. It was shown [25] that CTAB addition during mechanochemical treatment of SnCl_2 and NH_4HCO_3 promotes the formation of complex $\text{SnO}_2/\text{Sn}_6\text{O}_4(\text{OH})_4$, in which heterojunctions makes better activity. Template-assisted materials were also used for the photooxidation of dyes [26,27].

In the present work, template-assisted SnO_2 -based materials were obtained. CTAB was used for the pore structure evolution. The obtained materials were studied using spectroscopic, physicochemical, and electrochemical techniques. Their catalytic properties were studied in photoelectrocatalytic oxidation of water and methanol. The important role of porous structure was shown for the photoelectrochemical features of the materials.

2. Results

SEM analysis of the samples shows that the use of PS balls during synthesis leads to the formation of additional pores of 100–150 nm in size (Figure 1).

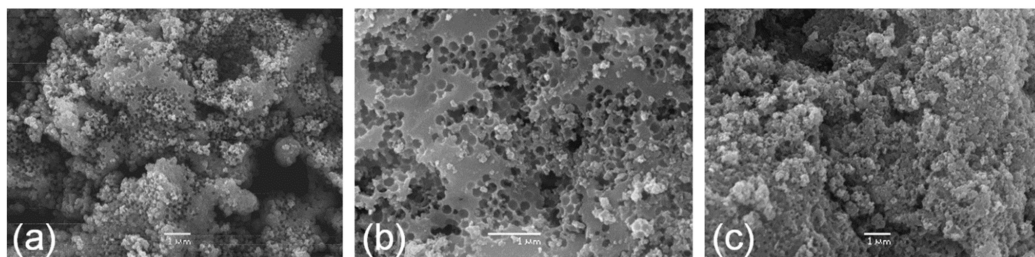


Figure 1. SEM analysis of samples TO2 (a), TO3 (b), and TO4 (c).

There was no increase in the pore volume but monomodal pore size distribution with average size 7 nm was characteristic of sample TO1 (Figure 2). An increase in the template content in samples TO2 and TO3 led to development of pore structure and bimodal pore size distribution with average sizes of 9 and 70 nm. The characteristic cavities from polystyrene balls were seen in SEM images (Figure 1). The 60 days aging (sample TO3) caused a narrow pore size distribution (Figure 2B). The structure of sample TO4 obtained with addition of CTAB was more friable than other samples (Figure 1c). A considerable pore volume in the range of 2 to 50 nm as well as macropores of 80–400 nm in size (Figure 2A) were characteristic of its pore structure. The sample had polymodal structure with maxima at 7, 14, 40 nm. BET specific surface area was practically independent of the amount of introduced template (samples TO1 and TO2) but decreased in samples obtained by aging (TO3) and CTAB addition (TO4) (Table 1). The maximal pore volume was observed in TO4 sample. We assume that the higher pore volume and the presence of macropores allow the photoelectrooxidation of organic substrate efficiency to be enhanced due to reduction of diffusion limitations.

According to Table 1, the conductivity of the samples increased with an increase in the content of template introduced during synthesis, while it decreased more upon aging during synthesis than upon CTAB addition.

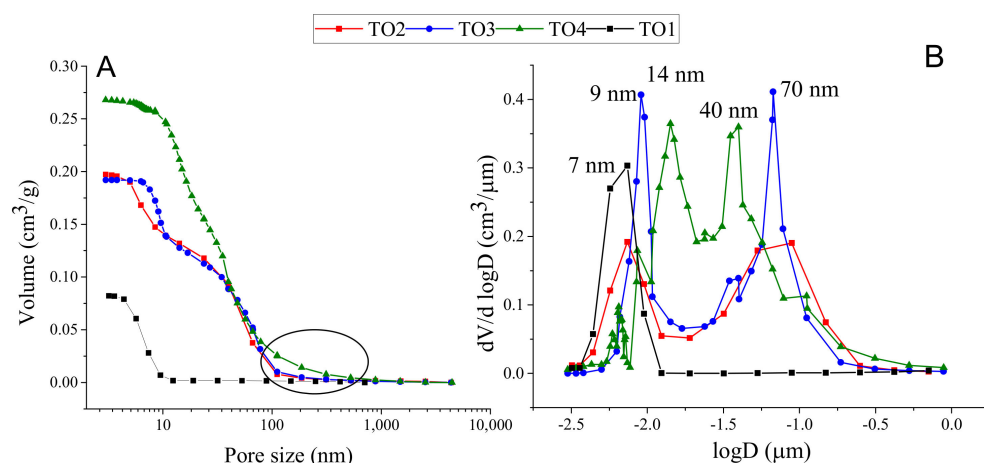


Figure 2. Mercury intrusion porosimetry data on pore volume (A) and pore size (B) distributions.

Table 1. Physicochemical properties of SnO₂ samples obtained from SnCl₄.

Sample	S _{BET} , m ² /g	V _{pore} , cm ³ /g	D _{pore} , nm	σ, mS/cm
TO1	47.7	0.093	12	0.27 ± 0.02
TO2	44.7	0.123	17	1.8 ± 0.4
TO3	30.6	0.099	19	0.8 ± 0.1
TO4	38.4	0.156	111	1.3 ± 0.2

S_{BET}—BET specific surface area, V_{pore}—pore volume, D_{pore}—average, σ—conductivity was measured at pressure 1.1 MPa.

According to XRD data, all the samples consisted only of the cassiterite phase (Figure 3). Rietveld refinement showed (Table 2, Figure S1) an increase in the average coherent scattering region (CSR) sizes from 5.9 to 6.5 and 8.6 nm with increasing template content and aging time, respectively. Again, CSR size increased (10.8 nm) when CTAB and large template proportions were used. Another kind of dependence was characteristic of the crystal structure defects (microstrain level): the wider CSR, the more crystal defects.

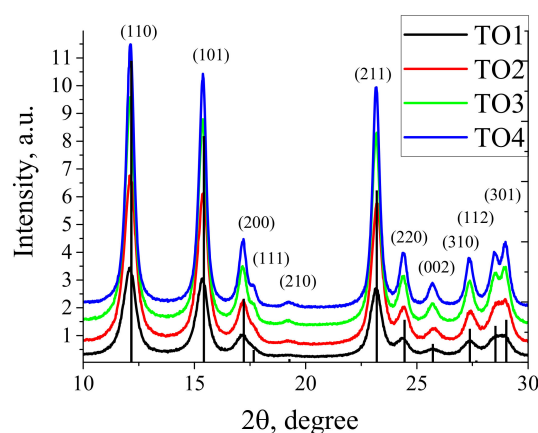


Figure 3. XRD data. Vertical lines are reflection positions of SnO₂ cassiterite phase (PDF #41-1445).

XPS data show the presence of oxygen and tin on the surface (Figure 4). Sn3d binding energies of the samples were 486.9/495.4 eV for TO1, 487.1/495.6 eV for TO2, 487.0/495.5 eV for TO3, and 487.0/495.4 eV for TO4. Similar values were obtained for SnO₂: 486.8 eV for Sn3d_{5/2} and 495.4 eV for Sn3d_{3/2} [28]. Peaks difference is 8.5 eV, which corresponds to tin oxide, SnO₂ [28,29]. O1s binding energy was 530.9 eV for all the samples.

Table 2. Accurate parameters of structure and microstructure of tin oxide phase samples under study. Standard deviation in last sign pointed in brackets. The table shows data on the coherent scattering region (CSR size), microstrains (ϵ), R-factor (R_{wp}) and the χ^2 criterion.

Sample	Cell Parameters, Å		Cell Volume, Å ³	CSR Size, nm	Microstrains, ϵ	R_{wp} , %	χ^2
	a	c					
TO1	4.742 (1)	3.191 (1)	71.75 (5)	5.9 (3)	0.14 (3)	5.3	1.4
TO2	4.735 (1)	3.185 (1)	71.40 (5)	6.5 (3)	0.12 (2)	4.9	1.8
TO3	4.743 (1)	3.191 (1)	71.78 (5)	8.6 (1)	0.11 (1)	4.7	1.8
TO4	4.743 (1)	3.190 (1)	71.76 (5)	10.8 (3)	0.09 (1)	5.0	1.9

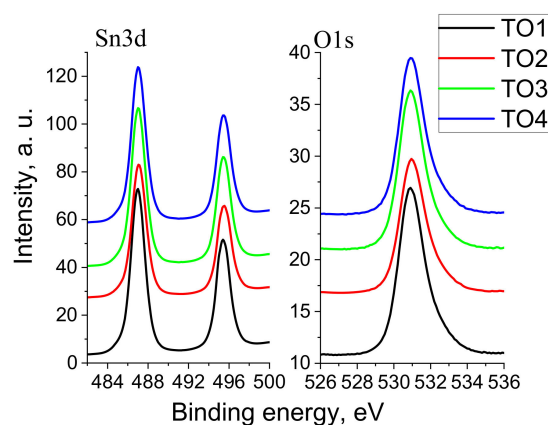


Figure 4. XPS data on Sn3d (left) and O1s (right).

Decomposition of peak Sn3d_{5/2} gave two bands at 485.0–485.2 eV and 487.0–487.1 eV (Figure S2). The first band is close to literature data on binding energies in tin metal at 484.9 eV [30,31], 484.5–484.9 eV [32], and 484.4 eV [33]. The data are presented in Table 3.

Table 3. Surface composition according to XPS data.

Sample	Components Sn3d, %		Components O1s, %		O_{Σ}/Sn_{Σ} Ratio
	Sn ⁰ (485.1 ± 0.1)	Sn ⁴⁺ (487.1 ± 0.1)	=O (531.0 ± 0.1)	-OH (532.4 ± 0.1)	
TO1	1.4	98.6	84.9	15.1	1.19
TO2	2.4	97.6	83.1	16.9	1.20
TO3	2.4	97.6	83.9	16.1	1.20
TO4	2.1	97.9	82.3	17.7	1.19

In our case, the peak Sn3d_{5/2} is slightly shifted towards higher binding energies, supposedly, due to the positive charge on Sn. The second band corresponds to Sn⁴⁺ which, according to literature data, falls into the region of 487.2–487.5 [30,31], 484.5–484.9 eV [32], and 484.4 eV [33]. Decomposition of O1s peak also gave two bands at 530.9 and 532.4 eV assigned to lattice oxygen SnO₂ [29,34,35] and to hydroxylated surface species, respectively. According to literature data, binding energies of the species are 532.1–532.6 eV [30] and 532.7 eV [36]. The presence of reduced species could be accounted for by partial reduction of Sn⁴⁺ during decomposition of template despite the presence of oxygen atmosphere. In addition, Sn⁰ peaks were not identified in the XRD spectra that indicate the absence of the Sn phase.

UV–Vis spectroscopy data (Figure 5B) show the maximum of absorption in all the samples at ca. 250 nm with tail to 360 nm that is typical of tin oxide. Although tin oxide

is a direct transition semiconductor, literature data also argue for indirect transitions [37]. Band gaps for indirect ($n = 2$, Figure 5C) and direct ($n = 1/2$, Figure 5D) transitions were calculated by Formula (1):

$$(\alpha h\nu)^{\frac{1}{n}} = A(h\nu - E_g) \quad (1)$$

where α is absorption coefficient, h is the Planck constant, ν is frequency, A is parameter, and E_g is band gap.

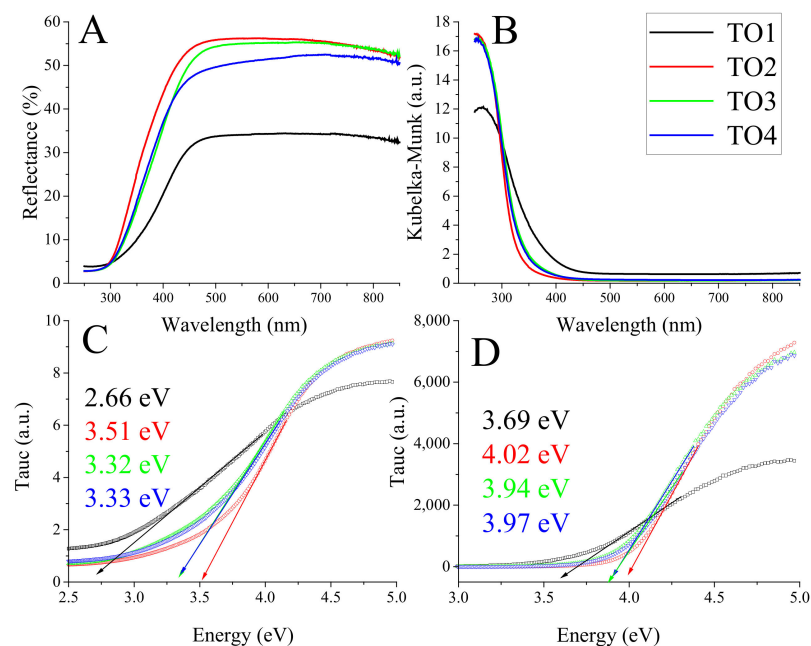


Figure 5. UV-Vis DRS data: DRS spectra (A); absorption spectra obtained by Kubelka–Munk converting (B); Tauc plot calculated for indirect transition (C); Tauc plot calculated for direct transition (D).

E_g values for indirect and direct transitions were 2.66 and 3.69 eV for TO1, 3.51 and 4.02 eV for TO2, 3.32 and 3.94 eV for TO3, and 3.33 and 3.97 eV for TO4. The values obtained are typical of tin oxide [37,38]. Increasing the template content during synthesis increased band gap (samples TO1 and TO2). Ageing during synthesis (sample TO3) decreased considerably band gap for the indirect transitions and almost did not change it for the direct transitions. An increase in the template content and CTAB addition during synthesis (sample TO4) had no influence on the measured values.

Structure of the samples was studied by Raman spectroscopy (Figure 6).

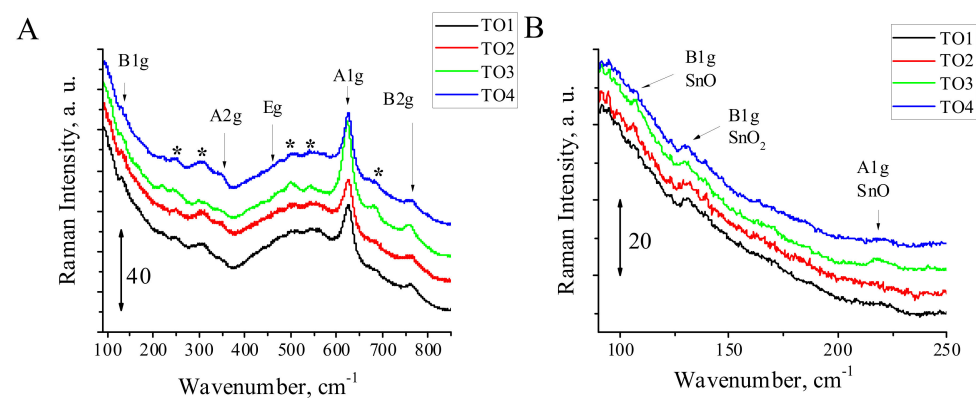


Figure 6. Raman spectra of samples (A) and magnified region for range 100–250 cm^{-1} (B). Volume (specified by arrows) and surface (specified by asterisks) modes correspond to SnO_2 . Vibration modes of SnO are depicted in (B).

Spectra of all the samples contain peaks typical of volume vibrations of SnO_2 : 625 cm^{-1} (A1g), 762 cm^{-1} (B2g), 472 cm^{-1} (Eg), and 132 cm^{-1} (B1g) [39–41]. Numbers of asterisks marked peaks with low intensity correspond to phonon surface vibrations. Their detailed analysis is presented in Table S1. Spectra (Figure 6B) showed the presence of a very small contribution of SnO (peaks: 107 cm^{-1} –B1g and 217 cm^{-1} –A1g). The spectra include a broad band with the maximum at 573 cm^{-1} . According to literature data, the band is assigned to surface defects [42–44].

From the obtained physicochemical results, it is reasonable to conclude that the material structures and surface properties are similar; there are only minor differences in nanoparticles and degree of crystal tension. The most differences are observed in pore structures.

2.1. Flat-Band Potentials Determination

In more than 95% of cases, the Mott–Schottky approach was used for flat-band determination of semiconductors [45]. A number of limitations for the method make a wide range of determined values [45–47]. The use of several methods was suggested for accurate analysis: (1) Mott–Schottky analysis, (2) Gartner–Butler analysis, (3) open circuit potential measurements, and (4) photocurrent onset potential, as well as addition of sacrificial agents for suppression of charge recombination [46,47]. We used all the methods for detailed studies of flat-band potentials and methanol was chosen as the sacrificial agent. Since the use of the Gartner–Butler method in our research led to unreliable consequences, we used potential of photocurrent beginning. The obtained results are presented in Figures S4–S7 and Table 4.

Table 4. Flat-band potentials (V, RHE) determined by methods: Photocurrent beginning (C—cathodic, A—anodic), Mott–Schottky, open circuit potential (OCP), photocurrent onset (C—cathodic, A—anodic) at chopped illumination (3 s).

№	Sample	Photocurrent		Mott–Schottky	OCP	Photocurrent Onset		Average
		C	A			C	A	
1	TO1	0.18	0.43 ¹	0.37	0.35	0.27	0.25	0.28 ± 0.08
2	TO1 + MeOH	0.48 ¹	0.19	0.31	0.12	0.09	0.09	0.16 ± 0.09
3	TO2	0.19	0.32	0.41 ¹	0.35	0.2	0.21	0.25 ± 0.08
4	TO2 + MeOH	0.18	0.30	0.3	0.24	0.14	0.15	0.22 ± 0.07
5	TO3	0.4 ¹	0.19	0.21	0.39	0.24	0.23	0.25 ± 0.08
6	TO3 + MeOH	0.17	0.35 ¹	0.06	0.27	0.13	0.13	0.15 ± 0.08
7	TO4	0.13	0.17	−0.01	0.21 ¹	0.09	0.09	0.09 ± 0.07
8	TO4 + MeOH	0.13	0.12	0.02	−0.05			0.06 ± 0.09

¹ Value was not used for estimation of average potential.

Detailed studies by a number of techniques will be the aim of the further research. Here we analyze the determined average values. Close average flat-band potentials (0.25–0.29 V) are characteristic of TO1, TO2, and TO3 in the absence of methanol. At the same time, a lower flat-band potential of 0.09 V was determined with sample TO4. With methanol as the sacrificial agent, the flat-band potentials decreased to 0.15–0.22 V for TO1, TO2, and TO3 and to 0.06 V for TO4. This was due to scavenging of photogenerated holes (recombination suppression). The other data measured under identical conditions showed scattering of values [45]. Detailed analysis of literature data on flat-band potential of tin oxides [45] revealed the average value in the range of $0.342 \pm 0.378\text{ V RHE}$. Our data agree well with the literature data.

In electrochemical studies, the samples changed their colors to light brown after scanning to negative potential field. Apparently, there was reversible reduction of tin oxide during the measurements. It was noted [48] that partial reduction of oxide as well as surface Faradaic processes may happen at scanning to cathodic potential field. Moreover, the formation of surface hydroxylated species under certain potentials could increase O/Sn ratio to 3 and change the measured capacity [49]. Scanning to anodic potential field could increase the quantity of surface oxygen and deviation of linearity Mott–Schottky plot [48]. Thus, the change in the oxidation state of tin could influence the position of flat-band potential. Reduction of samples also hinders measurements of onset potentials. For TO1 and especially for TO4, photocurrents in the presence of methanol did not fade scanning to cathodic direction (Figure S7). Potentials of TO4 measured by other methods also point out its reduction affinity.

2.2. Photoelectrocatalytic Properties

Figure 7 shows current density curves of samples TO1–TO4 (cell potentials: 0.4 V and 1.6 V RHE) at periodic illumination in the absence and in the presence of methanol.

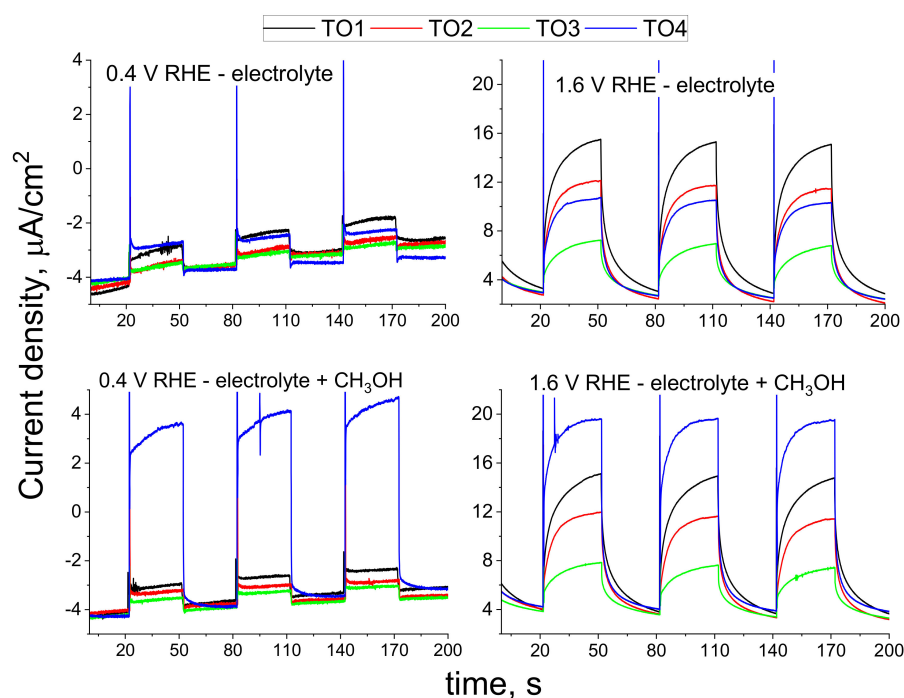


Figure 7. Time dependence of current density in TO1–TO4 at periodical illumination: 0.4 V (left) and 1.6 V (right) without (upper plots) and with methanol addition (bottom plots).

Low photocurrents are characteristic of TO1–TO3 at cell potential 0.4 V but higher photocurrent is characteristic of TO4. At high cell potential, 1.6 V photocurrents increase in the series TO3 < TO4 < TO2 < TO1. Methanol addition causes a considerable rise of photocurrent in the sample TO4 at both potentials (0.4 and 1.6 V). In literature, photocurrents were determined in borate buffer (pH = 7.5) at a potential of 600 V SCE (~0.8 V RHE). The maximum photocurrents were estimated as ca. 0.5 $\mu\text{A}/\text{cm}^2$ at the wavelength irradiation of 370 nm [50]. The photocurrents of 3.6 $\mu\text{A}/\text{cm}^2$ were reported for SnO_2 in 0.5 M Na_2SO_4 [51]. The photocurrents observed by us in the absence of methanol agree with the literature data. There are practically no literature data on photoelectrocatalytic oxidation of methanol on SnO_2 . Tin oxide is mainly used as the support for platinum catalysts for oxidation of methanol in direct methanol fuel cells. Hydroxyl groups formed on the surface of tin oxide during oxidation of methanol facilitates oxidation of CO on the surface of platinum [51,52]. Catalytic systems based on Pt/ SnO_2 /C show higher onset potential of the electrochemical

oxidation of methanol (0.6 V RHE) in 0.1 M HClO₄ [52]. The onset potential of methanol oxidation was -0.45 V Hg/HgO (about ~ 0.54 V RHE) with the Pt/SnO₂-C(100) system in the alkaline medium of 1 M NaOH [53] and 0.32 V vs. Ag/AgCl [54] with NiO-SnO₂/SO₄ in 1 M NaOH + 1 M CH₃OH. XPS studies of the gas-phase oxidation of methanol on SnO₂ showed that, depending on the degree of defectiveness and oxidation state of the surface, there can be two ways to achieve the reaction: with the breaking of the OH bond on the oxidized surface or with the breaking of the CO bond on the defective surface [55]. The photoelectrochemical oxidation of methanol in the 0.1 M Na₂SO₄ + 1M CH₃OH electrolyte was studied using TiO₂/ITO sample [56]. The observed currents were about 0.02 mA/cm² in a wide potential range from -0.1 to 1.4 V rel. Ag/AgCl. These values are close to those obtained in our work.

The dependence of photocurrent density on the potential applied in the range of 0.4–1.6 V was studied; the results are illustrated in Figure 8. The highest photocurrent was observed with TO4 at potentials below 0.7 V, and with TO1 at above 0.7 V. The photocurrent density of TO4 in the whole potential range under study upon addition of methanol. If we compare TO1 and TO2 catalysts with flat-band potentials, TO1 is more efficient to water and methanol oxidation. Evidently, despite more ramified pore structure and higher electroconductivity (1.8 mS/cm for TO2 and 0.27 mS/cm for TO1), the band gap plays a key role (3.69 eV for TO1 and 4.02 eV for TO2) and photocurrent is determined by a number of absorbed photons. Aging during synthesis (comparing TO2 and TO3 catalysts) leads to a decrease in the conductivity to 0.8 mS/cm, to narrowing of the band gap to 3.94 eV, and to a decrease in the photocurrent. The TO4 catalyst has closest conductivity (0.8 mS/cm) and band gap (3.97 eV) to those of TO2 and TO3 but more ramified pore and macropore structures, and its flat-band potential shifts to 0.14 V in the cathodic region against that of the other catalysts. TO4 shows higher photocurrent densities in the whole potential range under study.

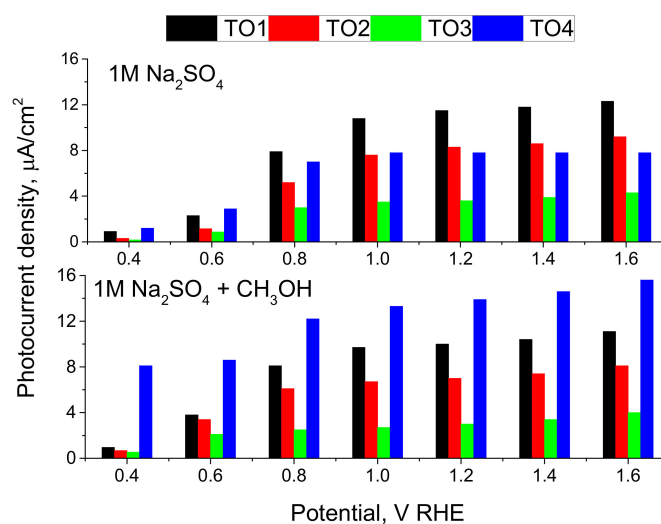


Figure 8. Photocurrent density dependence on potential without (upper plots) and with methanol (bottom plots).

As seen in Figure S8, the photocurrents become higher at potentials of 0.9 V for TO1 and TO2 and of 0.7 V for TO3 in the absence of methanol than upon addition of methanol to all of them except TO4. In the case of TO4, the photocurrent is higher in the presence of methanol in the whole potential range.

The energy band positions were obtained for the samples using average values of flat-band potentials and band gap of direct transitions are schematically presented in Figure S9. The value of the valence band potential for different materials can determine their activities as photoelectrocatalysts: the higher the potential, the higher the oxidation efficiency, provided that the recombination rates are similar. For samples characterized by developed

porous structure and similar values of the band gap positions (TO2–TO4), the valence band potentials (V RHE) decrease as follows: 4.25 (TO2) > 4.09 (TO3) > 4.03 (TO4), see Figure S9. However, the methanol oxidation activity is highest for the TO4 sample, which has the lowest valence band potential. The reasons for the higher activity may lie in the optimal pore structure and in the lower recombination rate. For the TO1 sample, in which the valence band potential is the lowest one (3.85 V RHE), high activities in the oxidation of water and methanol can be associated with a higher degree of photon absorption (Figure 5B).

3. Experimental

3.1. Materials

The following materials were used in the work: SnCl₄ (Reakhim, Moscow, Russia), cetyltrimethylammonium bromide (C₁₉H₄₂NBr) (Sigma-Aldrich, Inc., St. Louis, MO, USA), ethanol (Reakhim, Russia), ammonia solution (30 wt.%) (Baza №1 khimreaktivov, Moscow, Russia), Nafion (Sigma-Aldrich, Inc., St. Louis, MO, USA), methanol (Sigma-Aldrich, Inc., St. Louis, MO, USA), isopropanol (Reakhim, Russia), acetone (Reakhim, Russia), deionized water (conductivity 18 MΩ) produced by deionizer D-301 (Akvilon, Voronezh Oblast, Russia), and polystyrene (PS) microspheres (250 ± 30 nm in diameter) in the form of the water suspension named Latex hereinafter. The Latex was synthesized before according to work [57].

3.2. Synthesis of Tin Oxides

Synthesis of TO1: 20 mL of Latex (concentration 43.5 mg/mL) was mixed with 20 mL of ethanol (96%). Then, 10 mL of chilled SnCl₄ were poured in drops. In 20 min, tin oxide was precipitated by adding 14 mL of NH₃ solution. The precipitate was triply washed by centrifuging and calcined successively in flowing oxygen at 100 °C for 30 min, at 200 °C for 30 min, at 300 °C for an hour, at 400 °C for an hour, at 450 °C for two hours.

Synthesis of TO2 and TO3: 20 mL of Latex (concentration 100 mg/mL) was added to 20 mL of ethanol (96%) containing 10 g of polystyrene. Then, 10 mL of chilled SnCl₄ were poured in drop during 3–5 min under stirring. In half an hour, 28.5 mL of ammonia solution (30 wt.%) was dropped for precipitation of tin oxide. Then, the suspension was stirred for 1.5 h, centrifuged, and separated into two parts. One part (TO2 sample) was ultrasonically suspended in water and then centrifuged. Another part (TO3 sample) was aged in water for two months. Both precipitates were triply washed by ultrasonic dispersion and centrifuging and calcined in oxygen atmosphere; TO2 was calcined at 100 °C for 30 min, at 200 °C for 30 min, at 300 °C for an hour, at 400 °C for an hour, at 450 °C for two hours; TO3 at 450 °C for three hours, at 500 °C for three hours, at 530 °C for three hours.

Sample TO4: Suspension of 10 g PS and 1 g CTAB in 30 mL of ethanol (96%) was mixed with 30 mL of Latex (concentration 43.5 mg/mL), and 10 mL of SnCl₄ was dropped. In 30 min, the mixture was added to ammonia solution to achieve neutral pH. The precipitate was triply washed by ultrasonic dispersion and centrifugation and calcined in oxygen atmosphere at 450 °C for three hours, at 500 °C for three hours, at 530 °C for three hours.

Initial experiments showed that template oxidation is a difficult task for two reasons. First, the melting point of polystyrene is 170 °C. When heated fast enough, polystyrene, instead of being oxidized, can melt to cause distortion of the 3D structure. The second reason is the large amount of the template. Rapid heating can produce carbon instead of oxidizing it. Therefore, the stepwise heat treatment allowed certain times at each temperature for more efficient oxidation of polystyrene.

3.3. Physicochemical Characterization

The porous structure was characterized using nitrogen adsorption at 77 K with an ASAP 2400 specific surface analyzer (Micromeritics, Norcross, GA, USA). Oxide samples were treated at 573 K until the residual pressure of 10^{−3} mmHg was reached. Scanning electron microscopy (SEM) images were acquired using a JSM-6460LV microscope (JEOL Ltd., Peabody, MA, USA) with an accelerating voltage of 15–20 kV. X-ray patterns were ac-

quired using a STOE STADI MP diffractometer (STOE & Cie GmbH, Darmstadt, Germany) with MoK α radiation ($\lambda = 0.70926 \text{ \AA}$). A position-sensitive detector DECTRIS MYTHEN was used to register the signal. Scanning was carried out in the range of angles 2θ 3–50°, the accumulation time was 10 s. Full-profile modeling by the Rietveld method was carried out using the Topas V. 4.2 software package (Bruker, Bremen, Germany). The porous macrostructure of the catalysts was studied by mercury porosimetry using an AutoPore IV 9500 device (Micromeritics, Norcross, GA, USA) designed for measurements at the mercury pressure from 0.1 MPa to 414 MPa, which corresponds to a pore radius range from 7430 nm to 1.8 nm. The relative measurement error was no more than 2%. XPS spectra were acquired using a SPECS photoelectron spectrometer (SPECSGROUP, Berlin, Germany) with non-monochromatized AlK α irradiation ($h\nu = 1486.6 \text{ eV}$, 150 W). The elemental composition of impurities in the tin oxide samples was determined using a VARIO EL CUBE CHNS–O analyzer (Elementar Analysensysteme GmbH, Langenselbold, Germany). The data obtained were averaged upon at least three time analyses of each sample.

UV–Vis diffuse reflectance spectra (DRS) were acquired using a Cary 300 UV–Vis spectrophotometer from Agilent Technologies Inc. (Santa Clara, CA, USA) equipped with a DRA-30I diffuse reflectance accessory and special pre-packed polytetrafluoroethylene (PTFE) as the reflectance standard. Raman spectra were recorded using a Lab RAM HR spectrometer (Horiba, Longjumeau, France) equipped with an Olympus BX41 optical microscope, an argon laser (wavelength 488 nm) and a Symphony CCD detector (Artisan Technology group, Champaign, IL, USA) in backscattering geometry.

3.4. Electrochemical Characterization

Electrical resistance of samples was studied by electrochemical impedance spectroscopy at room temperature in the frequency range of 10 to 5×10^5 Hz. A weighed sample (~50 mg) was placed in a cell chamber between two metal electrodes, which were subjected to different pressures. The impedance spectra were recorded at pressure varied between 0.13 and 1.7 MPa. For comparison, the data are presented at the pressure of 1.1 MPa. Electrical conductivity was calculated by Formula (2):

$$\sigma = \frac{l}{R \cdot A} \quad (2)$$

where σ is the electrical conductivity, mS/cm, l is the distance between electrodes (cm), R is the resistance (Ω), and A is the area of the site (cm^2).

3.5. Photoelectrocatalytic Tests

Photoelectrochemical tests were carried out at 25 °C using a potentiostat Autolab PGSTAT302N (Metrohm AG, Herisau, Switzerland) with a frequency response analyzer. Electrolyte was 1 M Na₂SO₄, reference and counter electrodes were Hg/HgSO₄ and Pt, respectively. The working fluorinated tin oxide (FTO) glass electrode was coated with photocatalysts. Before the experiment, catalyst suspensions were supported on FTO by drop-casting followed by drying and thermal treatment (150 °C, 30 min). Catalyst suspensions were obtained by ultrasonification of 10 mg catalyst and 0.01 mg of Nafion (as ethanol solution) in 1 mL of deionized water. The source light was a UV light emitting diode (LED) with a maximum irradiation at 370 nm. Before measurement, catalysts supported on FTO were treated under irradiation for 30 min to oxidize organic impurities. In experiments where methanol was added to electrolyte, the concentration of methanol was 1 M. Photocurrent measurements were carried out in electrolyte as well as in the presence of methanol at the potential range of 0.4–1.6 V RHE during alternating light irradiation (3.3 mW/cm²) and dark for 30 s. Impedance measurements at different potentials of cell were recorded for frequency range 1–10,000 Hz with amplitude 10 mV. The capacity was calculated according to Equation (3):

$$C = (2\pi f Z'')^{-1} \quad (3)$$

where C is capacity, f is frequency, Z'' is imaginary impedance.

3.6. Flat-Band Potential Determination

For detailed study of flat-band potentials, as previously reported [46,47], the approaches were used based on four independent methods. For the Mott–Schottky method, Equation (4) was used:

$$C_{sc}^{-2} = 2 \left(N_d e_0 \epsilon_0 \epsilon_s S^2 \right)^{-1} \left(V - V_{fb} - \frac{kT}{e_0} \right) \quad (4)$$

where C_{sc} is depletion layer capacity, N_d is charge carriers density, e_0 is electron charge, ϵ_0 is vacuum permittivity, ϵ_s is dielectric constant of material, S is electrode surface area, V is potential, V_{fb} is flat-band potential, k is the Boltzmann constant, and T is temperature. According to Equation (4), the dependence of capacity on potential cell was plotted and linear approximation was implemented. Corresponding frequencies were chosen to show an insignificant influence on flat-band potential.

According to the Gartner–Butler method, the dependence of photocurrent (j_{photo}) on potential can be described by Equation (5):

$$j_{photo}^2 = (I_0 \alpha)^2 \frac{2e_0 \epsilon_0 \epsilon_s}{N_d} (V - V_{fb}) \quad (5)$$

Cyclic voltammograms (CV) were recorded (10 mV/s). Flat-band potential for anodic and cathodic curves can be estimated from linear dependence of j_{photo}^2 on potential applied.

Photocurrent onset potentials were determined from chopped illumination (3 s) when recording CV (1 mV/s). Flat-band potential was fixed when photocurrents fade.

For the open circuit potential (OCP) method, the cell potential was measured when catalysts were light irradiated (370 nm) with different power density from 3.3 to 190 mW/cm². Flat-band potentials were estimated by extrapolation of measured potentials data to infinite light power density.

4. Conclusions

A series of tin oxides were synthesized using different content of polystyrene balls (250 nm) as the template and CTAB for development of pore structure. The materials are studied by a number of physicochemical and photoelectrochemical methods, and their electroconductivities were determined. Mercury intrusion porosimetry and low-temperature nitrogen adsorption studies show that an increase in the template content leads to increasing in the specific pore volume and to the formation of bimodal structure of pores of 9 and 70 nm in size. According to the mercury intrusion porosimetry data, addition of CTAB and increasing template content results in the formation of trimodal mesopores structure with maximum sizes of 7, 14, and 40 nm as well as macropores of 80–400 nm in size. According to the low-temperature nitrogen adsorption data, the average pore sizes increased from 19 to 111 nm. All materials are cassiterite phase with coherent scattering region (CSR) of 5.9–10.8 nm. XPS studies reveal the presence of little quantities of reduced Sn (1.4–2.4%) and hydroxylated (15.1–17.7%) species on the surface of SnO₂. Raman spectroscopic studies showed the possible presence of small quantities of SnO. The Mott–Schottky method, chopped-illumination method, open circuit potential dependence from light irradiation and potential of photocurrent appearance were used to estimate the flat-band potentials of the materials in the absence and in the presence of sacrificial agent (methanol). It was shown that addition of methanol leads to a decrease in the potential to 0.1–0.03 V due to decreasing recombination rate. Flat-band potentials measured in the methanol added electrolyte were similar in all the samples except TO4, prepared at high template content with CTAB addition, and fell into the range of 0.15–0.22 V RHE. The lower flat-band potential of TO4 sample (0.06 V RHE) was presumably due to the porous structure effect.

Photoelectrocatalytic properties of the samples to oxidation of water and methanol were studied at potential range 0.4–1.6 V RHE. It was shown that the catalyst obtained by addition of CTAB exhibited higher photocurrents in the methanol oxidation. The higher current could be the result of a ramified macro-meso-porous structure that facilitated diffusion of methanol in the pores of material.

Supplementary Materials: The following supporting information can be downloaded at: <https://www.mdpi.com/article/10.3390/catal13010168/s1>. Figure S1: XRD data for samples TO1 (1), TO2 (2), TO3 (3), and TO4 (4). Figure S2: XPS data of samples TO1 (1), TO2 (2), TO3 (3), and TO4 (4) with peak decompositions for Sn3d5/2 and O1s. Figure S3: Raman spectra of samples in the region 440–600 cm⁻¹. Table S1: Comparison of bands in Raman spectra with literature data. Figure S4: Current curves of CV (scan rate—10 mV/s) in dark (black) and under irradiation (red) for the samples TO1 (1), TO2 (2), TO3 (3), and TO4 (4) in electrolyte (upper plots) and with methanol addition (lower plots). Figure S5: Mott–Schottky plots for dark capacity measurements of samples: TO1 (1), TO2 (2), TO3 (3), and TO4 (4) in electrolyte (A) and with methanol addition (B). Figure S6: Open circuit potential dependence from light irradiation intensity for samples TO1 (1), TO2 (2), TO3 (3), and TO4 (4) in electrolyte (black points) and with methanol addition (red points). Figure S7: Current curves of CV (scan rate—1 mV/s) at chopped illumination for the samples TO1 (1), TO2 (2), TO3 (3), and TO4 (4) in electrolyte (a) and with methanol addition (b). Figure S8: Dependence of photocurrent density from potential in electrolyte (black) and with methanol addition (red) for the samples TO1–TO4. Figure S9: Energy band diagram of samples based on average flat-band potentials and band gaps for direct transitions. Refs. [39–41,58–60] are cited in Supplementary Materials.

Author Contributions: Conceptualization, funding acquisition, supervision, writing—original draft: E.G., formal analysis, methodology: E.G. and E.K., writing—review and editing E.G., E.K. and V.P., investigation: E.K. and I.C. All authors have read and agreed to the published version of the manuscript.

Funding: This work was supported by the Russian Science Foundation (grant no. 22-23-20208) and the Novosibirsk region (agreement no. p-21 dated 6 April 2022).

Data Availability Statement: The processed data required to reproduce these findings are available by e-mail to the corresponding author.

Acknowledgments: Evgeniy Losev (Novosibirsk State University) for Raman spectra recording.

Conflicts of Interest: The authors declare no conflict of interest.

References

1. Sharma, A.; Ahmed, A.; Singh, A.; Oruganti, S.K.; Khosla, A.; Arya, S. Review—Recent Advances in Tin Oxide Nanomaterials as Electrochemical/Chemiresistive Sensors. *J. Electrochem. Soc.* **2021**, *168*, 027505. [\[CrossRef\]](#)
2. Reddy, M.V.; Linh, T.T.; Hien, D.T.; Chowdari, B.V.R. SnO₂ Based Materials and Their Energy Storage Studies. *ACS Sustain. Chem. Eng.* **2016**, *4*, 6268–6276. [\[CrossRef\]](#)
3. Dalapati, G.K.; Sharma, H.; Guchhait, A.; Chakrabarty, N.; Bamola, P.; Liu, Q.; Saianand, G.; Sai Krishna, A.M.; Mukhopadhyay, S.; Dey, A.; et al. Tin oxide for optoelectronic, photovoltaic and energy storage devices: A review. *J. Mater. Chem. A* **2021**, *9*, 16621–16684. [\[CrossRef\]](#)
4. Sun, C.; Yang, J.; Xu, M.; Cui, Y.; Ren, W.; Zhang, J.; Zhao, H.; Liang, B. Recent intensification strategies of SnO₂-based photocatalysts: A review. *Chem. Eng. J.* **2022**, *427*, 131564. [\[CrossRef\]](#)
5. Mishra, S.R.; Ahmaruzzaman, M. Tin oxide based nanostructured materials: Synthesis and potential applications. *Nanoscale*. **2022**, *14*, 1566–1605. [\[CrossRef\]](#)
6. Dhanalakshmi, M.; Saravanakumar, K.; Lakshmi Prabavathi, S.; Abinaya, M.; Muthuraj, V. Fabrication of novel surface plasmon resonance induced visible light driven iridium decorated SnO₂ nanorods for degradation of organic contaminants. *J. Alloys Compd.* **2018**, *763*, 512–524. [\[CrossRef\]](#)
7. Tang, J.J.; Zhao, T.P.; Li, Z.H.; Xiao, Q.Z.; Lei, G.T.; Gao, D.S. Preparation and electrochemical study of three-dimensional ordered macroporous SnO₂ material for lithium ion batteries. *Nanosci. Nanotechnol. Lett.* **2012**, *4*, 185–190. [\[CrossRef\]](#)
8. Yim, C.H.; Baranova, E.A.; Courtel, F.M.; Abu-Lebdeh, Y.; Davidson, I.J. Synthesis and characterization of macroporous tin oxide composite as an anode material for Li-ion batteries. *J. Power Sources* **2011**, *196*, 9731–9736. [\[CrossRef\]](#)
9. Li, Z.; Tan, Y.; Huang, X.; Zhang, W.; Gao, Y.; Tang, B. Three-dimensionally ordered macroporous SnO₂ as anode materials for lithium ion batteries. *Ceram. Int.* **2016**, *42*, 18887–18893. [\[CrossRef\]](#)

10. Hashimoto, M.; Inoue, H.; Hyodo, T.; Shimizu, Y.; Egashira, M. Preparation and gas sensor application of ceramic particles with submicron-size spherical macropores. *Sens. Lett.* **2008**, *6*, 887–890. [[CrossRef](#)]
11. Park, N.K.; Lee, T.H.; Kim, M.J.; Lee, T.J. Preparation of macroporous semiconductive materials for the sensing of sulfur compounds. *Sens. Mater.* **2015**, *27*, 61–68.
12. Nonaka, S.; Hyodo, T.; Shimizu, Y.; Egashira, M. Preparation of macroporous semiconductor gas sensors and their odor sensing properties. *IEEE Trans. Sens. Micromach.* **2008**, *128*, 141–144. [[CrossRef](#)]
13. Hyodo, T.; Sasahara, K.; Shimizu, Y.; Egashira, M. Preparation of macroporous SnO₂ films using PMMA microspheres and their sensing properties to NO_x and H₂. *Sens. Actuators B Chem.* **2005**, *106*, 580–590.
14. Yuan, L.; Hyodo, T.; Shimizu, Y.; Egashira, M. Preparation of Mesoporous and meso-macroporous SnO₂ powders and application to H₂ gas sensors. *Sens. Mater.* **2009**, *21*, 241–250.
15. Wang, J.; Xu, Y.; Xu, W.; Zhang, M.; Chen, X. Simplified preparation of SnO₂ inverse opal for Methanol gas sensing performance. *Microporous Mesoporous Mater.* **2015**, *208*, 93–97. [[CrossRef](#)]
16. Zhang, B.; Fu, W.; Li, H.; Fu, X.; Wang, Y.; Bala, H.; Wang, X.; Sun, G.; Cao, J.; Zhang, Z. Synthesis and characterization of hierarchical porous SnO₂ for enhancing ethanol sensing properties. *Appl. Surf. Sci.* **2016**, *363*, 560–565. [[CrossRef](#)]
17. Khalameida, S.; Samsonenko, M.; Skubiszewska-Zięba, J.; Zakutevskyy, O. Dyes catalytic degradation using modified tin(IV) oxide and hydroxide powders. *Adsorpt. Sci. Technol.* **2017**, *35*, 853–865. [[CrossRef](#)]
18. Fan, J.; Shi, H.; Xiao, H.; Zhao, G. Double-Layer 3D Macro-Mesoporous Metal Oxide Modified Boron-Doped Diamond with Enhanced Photoelectrochemical Performance. *ACS Appl. Mater. Interfaces* **2016**, *8*, 28306–28315. [[CrossRef](#)]
19. Li, K.N.; Wang, Y.F.; Xu, Y.F.; Chen, H.Y.; Su, C.Y.; Kuang, D.B. Macroporous SnO₂ synthesized via a template-assisted reflux process for efficient dye-sensitized solar cells. *ACS Appl. Mater. Interfaces* **2013**, *5*, 5105–5111. [[CrossRef](#)]
20. Chen, H.; Guo, A.; Huang, S.; Zhu, J.; Cheng, L. Enhanced removal of organic dyes from porous channel-like SnO₂ nanostructures. *Mater. Res. Express* **2017**, *4*, 055019. [[CrossRef](#)]
21. Zaraska, L.; Gawlak, K.; Gurgul, M.; Chlebda, D.K.; Socha, R.P.; Sulka, G.D. Controlled synthesis of nanoporous tin oxide layers with various pore diameters and their photoelectrochemical properties. *Electrochim. Acta* **2017**, *254*, 238–245. [[CrossRef](#)]
22. Zhu, Y.; Wang, L.; Huang, G.; Chai, Y.; Zhai, X.; Huang, W. Luminescent and photocatalytic properties of hollow SnO₂ nanospheres. *Mater. Sci. Eng. B Solid State Adv. Technol.* **2013**, *178*, 725–729. [[CrossRef](#)]
23. Xu, S.; Sun, F.; Gu, F.; Zuo, Y.; Zhang, L.; Fan, C.; Yang, S.; Li, W. Photochemistry-based method for the fabrication of SnO₂ monolayer ordered porous films with size-tunable surface pores for direct application in resistive-type gas sensor. *ACS Appl. Mater. Interfaces* **2014**, *6*, 1251–1257. [[CrossRef](#)] [[PubMed](#)]
24. Wang, D.-H.; Jia, L.; Wu, X.-L.; Lua, L.-Q.; Xu, A.-W. One-step hydrothermal synthesis of N-doped TiO₂/C nanocomposites with high visible light photocatalytic activity. *Nanoscale* **2012**, *4*, 576–584. [[CrossRef](#)] [[PubMed](#)]
25. Liang, B. Mechanical-induced spontaneous formation of SnO₂/Sn₆O₄(OH)₄ photocatalysts at room temperature. *Mater Lett.* **2019**, *252*, 155–157. [[CrossRef](#)]
26. Karunakaran, C.; Sakthi Raadha, S.; Gomathisankar, P. Microstructures and optical, electrical and photocatalytic properties of sonochemically and hydrothermally synthesized SnO₂ nanoparticles. *J. Alloys Compd.* **2013**, *549*, 269–275. [[CrossRef](#)]
27. Park, J.T.; Lee, C.S.; Kim, J.H. One-pot synthesis of hierarchical mesoporous SnO₂ spheres using a graft copolymer: Enhanced photovoltaic and photocatalytic performance. *RSC Adv.* **2014**, *4*, 31452–31461. [[CrossRef](#)]
28. Luque, P.A.; Nava, O.; Soto-Robles, C.A.; Chinchillas-Chinchillas, M.J.; Garrafa-Galvez, H.E.; Baez-Lopez, Y.A.; Valdez-Núñez, K.P.; Vilchis-Nestor, A.R.; Castro-Beltrán, A. Improved photocatalytic efficiency of SnO₂ nanoparticles through green synthesis. *Optik* **2020**, *206*, 164299. [[CrossRef](#)]
29. Babu, B.; Neelakanta Reddy, I.; Yoo, K.; Kim, D.; Shim, J. Bandgap tuning and XPS study of SnO₂ quantum dots. *Mater Lett.* **2018**, *221*, 211–215. [[CrossRef](#)]
30. Chuvankova, O.A.; Domashevskaya, E.P.; Ryabtsev, S.V.; Yurakov, Y.A.; Popov, A.E.; Koyuda, D.A.; Nesterov, D.N.; Spirin, D.E.; Ovsyannikov, R.Y.; Turishchev, S.Y. XANES and XPS investigations of surface defects in wire-like SnO₂ crystals. *Phys. Solid State* **2015**, *57*, 153–161. [[CrossRef](#)]
31. Kövér, L.; Kovács, Z.; Sanjinés, R.; Moretti, G.; Cserny, I.; Margaritondo, G.; Pálincás, J.; Adachi, H. Electronic structure of tin oxides: High resolution study of XPS and Auger spectra. *Surf. Interface Anal.* **1995**, *23*, 461–466. [[CrossRef](#)]
32. Jiménez, V.M.; Mejías, J.A.; Espinós, J.P.; González-Eliphe, A.R. Interface effects for metal oxide thin films deposited on another metal oxide II. SnO₂ deposited on SiO₂. *Surf. Sci.* **1996**, *366*, 545–555. [[CrossRef](#)]
33. Chang, S.; Vijayan, S.; Aindow, M.; Jursich, G.; Takoudis, C.G. Hydrogen annealing effects on local structures and oxidation states of atomic layer deposited SnO_x. *J. Vac. Sci. Technol. A Vac. Surf. Films.* **2018**, *36*, 031519. [[CrossRef](#)]
34. Sun, M.; Su, Y.; Du, C.; Zhao, Q.; Liu, Z. Self-doping for visible light photocatalytic purposes: Construction of SiO₂/SnO₂/SnO₂:Sn²⁺ nanostructures with tunable optical and photocatalytic performance. *RSC Adv.* **2014**, *4*, 30820–30827. [[CrossRef](#)]
35. Davar, F.; Salavati-Niasari, M.; Fereshteh, Z. Synthesis and characterization of SnO₂ nanoparticles by thermal decomposition of new inorganic precursor. *J. Alloys Compd.* **2010**, *496*, 638–643. [[CrossRef](#)]
36. Nagasawa, Y.; Choso, T.; Karasuda, T.; Shimomura, S.; Ouyang, F.; Tabata, K.; Yamaguchi, Y. Photoemission study of the interaction of a reduced thin film SnO₂ with oxygen. *Surf. Sci.* **1999**, *433*, 226–229. [[CrossRef](#)]

37. Spencer, J.A.; Mock, A.L.; Jacobs, A.G.; Schubert, M.; Zhang, Y.; Tadjer, M.J. A review of band structure and material properties of transparent conducting and semiconducting oxides: Ga₂O₃, Al₂O₃, In₂O₃, ZnO, SnO₂, CdO, NiO, CuO, and Sc₂O₃. *Appl. Phys. Rev.* **2022**, *9*, 011315. [[CrossRef](#)]
38. Summit, R.; Marley, J.A.; Borrelli, N.F. The ultraviolet absorption edge of stannic oxide (SnO₂). *J. Phys. Chem. Solids.* **1964**, *25*, 1465–1469. [[CrossRef](#)]
39. Gaur, L.K.; Chandra Mathpal, M.; Kumar, P.; Gairola, S.P.; Agrahari, V.; Martinez, M.A.R.; Aragon, F.F.H.; Soler, M.A.G.; Swart, H.C.; Agarwal, A. Observations of phonon anharmonicity and microstructure changes by the laser power dependent Raman spectra in Co doped SnO₂ nanoparticles. *J. Alloys Compd.* **2020**, *831*, 154836. [[CrossRef](#)]
40. Babu, B.; Talluri, B.; Gurugubelli, T.R.; Kim, J.; Yoo, K. Effect of annealing environment on the photoelectrochemical water oxidation and electrochemical supercapacitor performance of SnO₂ quantum dots. *Chemosphere* **2022**, *286*, 131577. [[CrossRef](#)]
41. Zaraska, L.; Gawlak, K.; Wiercigroch, E.; Malek, K.; Kozieł, M.; Andrzejczuk, M.; Marzec, M.M.; Jarosz, M.; Brzózka, A.; Sulka, G.D. The effect of anodizing potential and annealing conditions on the morphology, composition and photoelectrochemical activity of porous anodic tin oxide films. *Electrochim. Acta* **2019**, *319*, 18–30. [[CrossRef](#)]
42. Ilka, M.; Bera, S.; Kwon, S.H. Influence of surface defects and size on photochemical properties of SnO₂ nanoparticles. *Materials* **2018**, *11*, 904. [[CrossRef](#)] [[PubMed](#)]
43. Kar, A.; Olszówka, J.; Sain, S.; Sloman, S.R.I.; Montes, O.; Fernández, A.; Pradhan, S.K.; Wheatley, A.E.H. Morphological effects on the photocatalytic properties of SnO₂ nanostructures. *J. Alloys Compd.* **2019**, *810*, 151718. [[CrossRef](#)]
44. Liu, L.Z.; Wu, X.L.; Gao, F.; Shen, J.C.; Li, T.H.; Chu, P.K. Determination of surface oxygen vacancy position in SnO₂ nanocrystals by Raman spectroscopy. *Solid State Commun.* **2011**, *151*, 811–814. [[CrossRef](#)]
45. Patel, M.Y.; Mortelliti, M.J.; Dempsey, J.L. A compendium and meta-analysis of flatband potentials for TiO₂, ZnO, and SnO₂ semiconductors in aqueous media. *Chem. Phys. Rev.* **2022**, *3*, 011303. [[CrossRef](#)]
46. Beranek, R. (Photo)electrochemical methods for the determination of the band edge positions of TiO₂-based nanomaterials. *Adv. Phys. Chem.* **2011**, *2011*, 786759. [[CrossRef](#)]
47. Hankin, A.; Bedoya-Lora, F.E.; Alexander, J.C.; Regoutz, A.; Kelsall, G.H. Flat band potential determination: Avoiding the pitfalls. *J. Mater. Chem. A* **2019**, *7*, 26162–26176. [[CrossRef](#)]
48. Armstrong, N.R.; Lin, A.W.C.; Fujihira, M.; Kuwana, T. Electrochemical and Surface Characteristics of Tin Oxide and Indium Oxide Electrodes. *Anal. Chem.* **1976**, *48*, 741–750. [[CrossRef](#)]
49. Bressel, B.; Gerischer, H. Effect of surface hydrolysis at tin dioxide polycrystalline thin film electrodes on dye sensitization quantum efficiency. *Ber. Bunsenges. Phys. Chem. Chem. Phys.* **1983**, *87*, 398–403. [[CrossRef](#)]
50. Knapik, A.; Syrek, K.; Kozieł, M.; Zaraska, L. Cathodic deposition of SnO₂ layers on transparent conductive substrates and their photoelectrochemical activity. *J. Ind. Eng. Chem.* **2022**, *111*, 380–388. [[CrossRef](#)]
51. Sun, M.; Gong, Z.; Zhang, Z.; Li, Y.; Xie, D.; Wu, F.; Li, R. Dependence of photoelectrochemical water splitting for oriented-SnO₂ on Carrier behaviors: Concentration, depletion and transportation. *Thin Solid Film.* **2021**, *732*, 138794. [[CrossRef](#)]
52. Menshikov, V.S.; Novomlinsky, I.N.; Belenov, S.V.; Alekseenko, A.A.; Safronenko, O.I.; Guterman, V.E. Methanol, ethanol, and formic acid oxidation on new platinum-containing catalysts. *Catalysts* **2021**, *11*, 158. [[CrossRef](#)]
53. Anjos, R.P.R.; Santos, A.O.; Antoniassi, R.M.; Alves, O.C.; Ponzio, E.A.; Silva, J.C.M. The Effect of Tin Addition to Platinum Catalysts with Different Morphologies towards Methanol Electrooxidation in Alkaline Media. *ACS Appl. Energy Mater.* **2021**, *4*, 6253–6260. [[CrossRef](#)]
54. Gu, Y.; Gao, P.; Yu, Z.; Hu, Y.; Xu, Z.; Zhang, C.; Li, J.; An, Y. Honeycomb-like mesoporous NiO-SnO₂/SO₄²⁻ solid superacid for the efficient reaction of methanol oxidation. *Int. J. Electrochem. Sci.* **2020**, *15*, 2481–2498. [[CrossRef](#)]
55. Kawabe, T.; Tabata, K.; Suzuki, E.; Nagasawa, Y. Methanol adsorption on an oxidized and a reduced SnO₂ thin film. *Surf. Sci.* **2000**, *454*, 374–378. [[CrossRef](#)]
56. Pablos, C.; Marugán, J.; van Grieken, R.; Adán, C.; Riquelme, A.; Palma, J. Correlation between photoelectrochemical behaviour and photoelectrocatalytic activity and scaling-up of P25-TiO₂ electrodes. *Electrochim. Acta* **2014**, *130*, 261–270. [[CrossRef](#)]
57. Parkhomchuk, E.V.; Semeykina, V.S.; Sashkina, K.A.; Okunev, A.G.; Lysikov, A.I.; Parmon, V.N. Synthesis of polystyrene beads for hard-templating of three-dimensionally ordered macroporosity and hierarchical texture of adsorbents and catalysts. *Top. Catal.* **2017**, *60*, 178–189. [[CrossRef](#)]
58. Lan, T.; Li, C.W.; Fultz, B. Phonon anharmonicity of rutile SnO₂ studied by Raman spectrometry and first principles calculations of the kinematics of phonon-phonon interactions. *Phys. Rev. B Condens. Matter Mater. Phys.* **2012**, *86*, 134302. [[CrossRef](#)]
59. Xiong, C.; Xiong, Y.; Zhu, H.; Zhang, Y.; Liu, Y. Investigation of Raman spectrum for nano-SnO₂. *Sci. China Ser. A Math. Phys. Astron.* **1997**, *40*, 1222–1227. [[CrossRef](#)]
60. Batzill, M.; Diebold, U. The surface and materials science of tin oxide. *Prog. Surf. Sci.* **2005**, *79*, 47–154. [[CrossRef](#)]

Disclaimer/Publisher's Note: The statements, opinions and data contained in all publications are solely those of the individual author(s) and contributor(s) and not of MDPI and/or the editor(s). MDPI and/or the editor(s) disclaim responsibility for any injury to people or property resulting from any ideas, methods, instructions or products referred to in the content.